Improved Subthalamic Nucleus Depiction with Quantitative Susceptibility Mapping[1]

Tian Liu, PhD
Sarah Eskreis-Winkler, MD
Andrew D. Schweitzer, MD
Weiwei Chen, MD, PhD[2]
Michael G. Kaplitt, MD, PhD
A. John Tsiouris, MD
Yi Wang, PhD

Purpose: To assess quantitative susceptibility mapping (QSM) in the depiction of the subthalamic nucleus (STN) by using 3-T magnetic resonance (MR) imaging.

Materials and Methods: This study was HIPAA compliant and institutional review board approved. Ten healthy subjects (five men, five women; mean age, 24 years ± 3 [standard deviation]; age range, 21–33 years) and eight patients with Parkinson disease (five men, three women; mean age, 57 years ± 14; age range, 25–69 years) who were referred by neurologists for preoperative navigation MR imaging prior to deep brain stimulator placement were included in this study. T2-weighted (T2w), T2*-weighted (T2*w), R2* mapping (R2*), phase, susceptibility-weighted (SW), and QSM images were reconstructed for STN depiction. Qualitative visualization scores of STN and internal globus pallidus (GPi) were recorded by two neuroradiologists on all images. Contrast-to-noise ratios (CNRs) of the STN and GPi were also measured. Measurement differences were assessed by using the Wilcoxon rank sum test and the signed rank test.

Results: Qualitative scores were significantly higher on QSM images than on T2w, T2*w, R2*, phase, or SW images ($P < .05$) for STN and GPi visualization. Median CNR was 6.4 and 10.7 times higher on QSM images than on T2w images for differentiation of STN from the zona incerta and substantia nigra, respectively, and was 22.7 and 9.1 times higher on QSM images than on T2w images for differentiation of GPi from the internal capsule and external globus pallidus, respectively. CNR differences between QSM images and all other images were significant ($P < .01$).

Conclusion: QSM at 3-T MR imaging performs significantly better than current standard-of-care sequences in the depiction of the STN.

Supplemental material: *http://radiology.rsna.org/lookup/suppl/doi:10.1148/radiol.13121991/-/DC1*

[1] From the Departments of Radiology (T.L., S.E., A.D.S., W.C., A.J.T., Y.W.) and Neurological Surgery (M.G.K.), Weill Cornell Medical College, 525 E 68th St, Box 141, New York, NY, 10021. Received September 4, 2012; revision requested October 24; revision received January 9, 2013; accepted February 5; final version accepted February 26. **Address correspondence to** Y.W. (e-mail: *yiwang@med.cornell.edu*).

[2] **Current address:** Tongji Hospital, Tongji Medical College, Huazhong University of Science and Technology, Wuhan, Hubei, China.

The subthalamic nucleus (STN) is a common surgical target of deep brain stimulation, which is an accepted surgical treatment for advanced Parkinson disease. This treatment has been proved to be effective in ameliorating bradykinesia, rigidity, tremor, and other functional impairments common in patients with advanced Parkinson disease (1,2). Deep brain stimulation consists of implanting a stimulating electrode in the brain, and the dorsolateral portion of the STN involved in the sensorimotor circuits has been identified as an ideal target (3). The precise identification of the STN target is paramount for maximizing therapeutic benefits while minimizing side effects, such as muscle contraction, dizziness, mood changes, and akinesias, which occur when the electrode is placed inappropriately (4–6). Thus, preoperative imaging is mandatory in surgical planning to minimize the surgical risks (7).

Direct visualization of the STN is challenging with current clinical magnetic resonance (MR) imaging sequences. The STN is a lens-shaped structure that is smaller than 1.5 cm, biconvex in the coronal plane, located in the caudal subthalamic region, and bordered superiorly by the zona incerta (ZI) and lenticular fasciculus and inferiorly by the substantia nigra (SN) (8). Although the STN appears to be hypointense on T2-weighted (T2w) images, presumably due to iron deposition (9), direct visualization may require ultrahigh-field-strength imagers, such as 7- or 9.4-T units (8,10,11) that have not been approved for use in routine clinical practice. Instead, navigation software is used to superimpose a stereotactic atlas on T2w images or to create the stereotactic target (12). Nevertheless, there is significant variability in the location of the STN in different patients with respect to both anatomic landmarks (anterior and posterior commissures) and stereotactic atlases (ventral intermedius nucleus of the thalamus or internal segment of the globus pallidus).

Quantitative susceptibility mapping (QSM) is an MR technique with novel tissue contrast that has shown promise in depicting deep brain nuclei in recent studies (13–16). QSM reflects the degree of polarization of local tissue in the magnetic field. This tissue magnetic susceptibility property is fundamentally different from traditional water relaxation or motion contrast in MR imaging and is primarily determined by tissue electron clouds and unpaired electrons in metallic elements of biomolecules, and deep brain nuclei are often associated with high iron concentration (9). In this work, we propose to assess QSM in the depiction of the STN by using 3-T MR imaging.

Advances in Knowledge

- The subthalamic nucleus (STN) appears hyperintense to normal-appearing white matter on quantitative susceptibility mapping (QSM) images, indicating paramagnetism likely resulting from iron deposition.
- The STN and substantia nigra (SN) can be readily differentiated on QSM images in the coronal plane.
- QSM provides the contrast-to-noise (CNR) ratio (median CNR = 3.10) needed to differentiate STN and SN; this was significantly higher than the CNR provided by T2-weighted, T2*-weighted, R2*, phase, or susceptibility-weighted imaging (median CNR = 0.29, 0.48, 0.54, 1.54, and 0.93, respectively; $P <$ .01 for each).

Materials and Methods

Subjects

This study was approved by the institutional review board, and written informed consent was obtained before MR imaging. This study included 10 healthy volunteers and eight patients, resulting in a sample size of 18 subjects. From September 1, 2011, to November 1, 2011, 10 healthy young volunteers (five men, five women; age range, 21–33 years; mean age, 24 years ± 3 [standard deviation]) were recruited from medical students. None of the volunteers had a history of *(a)* neurologic, psychiatric, or cardiovascular conditions; *(b)* concussion or brain surgery; or *(c)* drug or alcohol abuse. To demonstrate the clinical practicality, nine consecutive patients with Parkinson disease who *(a)* were admitted to our hospital from November 1, 2011, to November 30, 2012; *(b)* were referred by our neurologists for preoperative MR imaging prior to deep brain stimulator placement; and *(c)* underwent imaging with our STN protocol were included in this study. One patient was excluded because of an incomplete data set. The remaining eight patients were included in the analysis (five men, three women; mean age, 57 years ± 14; age range, 25–69 years).

Implication for Patient Care

- QSM may assist neurosurgeons in targeting the precise location of the STN in surgical planning for deep brain stimulator placement used to treat Parkinson disease.

Published online before print
10.1148/radiol.13121991 **Content code:** NR

Radiology 2013; 269:216–223

Abbreviations:
CNR = contrast-to-noise ratio
GPe = external globus pallidus
GPi = internal globus pallidus
IC = internal capsule
QSM = quantitative susceptibility mapping
SN = substantia nigra
STN = subthalamic nucleus
SW = susceptibility weighted
T2*w = T2* weighted
T2w = T2 weighted
ZI = zona incerta

Author contributions:
Guarantor of integrity of entire study, Y.W.; study concepts/study design or data acquisition or data analysis/interpretation, all authors; manuscript drafting or manuscript revision for important intellectual content, all authors; approval of final version of submitted manuscript, all authors; literature research, T.L., S.E., A.D.S., W.C.; clinical studies, S.E., W.C., M.G.K., A.J.T.; statistical analysis, T.L., S.E., W.C.; and manuscript editing, all authors

Funding:
This research was supported by the National Institutes of Health (grants R01EB013443-01 and R01NS072370).

Conflicts of interest are listed at the end of this article.

Imaging Protocol and Data Reconstruction

MR examinations were performed with a 3-T MR system (Signa HDxt; GE Medical Systems, Milwaukee, Wis) and an eight-channel head coil. Axial T1-weighted images were acquired in all subjects prior to imaging of the STN. This was a part of the routine imaging protocol for patients and was used to confirm that the volunteers had no focal lesions and had not undergone prior surgery. Afterward, standard-of-care sequences, including two-dimensional T2w imaging and three-dimensional T2*-weighted (T2*w) imaging, were respectively performed with a fast spin-echo sequence (repetition time msec/echo time msec, 8000/86; bandwidth, range, -62.5 to 62.5 kHz; four signals acquired) and a multiecho gradient-echo sequence (45/4.0, 7.6, 11.2, 14.8, 18.4, 22.0, 25.6, 29.2, 32.8, 36.4, 40.0; bandwidth range, -62.5 to 62.5 kHz; flip angle, 15°; one signal acquired). Both acquisitions had an identical field of view (24 × 19 × 8–10 cm), spatial resolution (0.75 × 0.75 × 2 mm), and spatial prescription for STN depiction, leading to a total of 40–50 sections. Images were acquired in the coronal plane perpendicular to the anterior commissure–posterior commissure line (or AC-PC line) so that important structures, such as the ventricles, STN, and SN could be seen in the same plane. The imaging time for both acquisitions was approximately 5 minutes or less.

The gradient-echo sequence, which spends about 80% of the total imaging time on data acquisition, yields rich information for different reconstruction strategies. A T2*w image was reconstructed by taking the square root of the sum of squares of the magnitude images from all the echoes; this square root of the sum of squares was a signal-to-noise ratio–weighted sum over all echoes and was similar to a contrast-to-noise ratio (CNR)-weighted sum previously proposed (17). An R2* mapping (hereafter, R2*) image was estimated with monoexponential fitting of the signal decay over echoes. A high-pass filtered phase image (hereafter, phase image) was created with the homodyne high-pass filtering method (18) on the complex data set by using one echo at an echo time of 26 msec (19) with a filter kernel size of 64 × 64. A susceptibility-weighted (SW) image was generated by multiplying the magnitude image at an echo time of 26 msec with a normalized phase image raised to the fourth power. A QSM image was generated by using the morphology-enabled dipole inversion with the nonlinear formulation method (14,15,20). All these images were calculated offline by using in-house software implemented in C++. All postprocessing of R2*, phase, SW, and QSM images was fully automatic without user intervention to eliminate operator bias.

Qualitative Image Analysis

The T2w images, as well as the previously mentioned T2*w, R2*, phase, SW, and QSM images, were assessed by two experienced neuroradiologists (A.J.T., W.C.; 15 and 10 years of neuroradiology experience, respectively) independently for STN visibility. In addition to STN, internal globus pallidus (GPi), which is another deep brain stimulation target used to treat Parkinson disease and dystonia, was also inspected. Coronal brain sections of each subject obtained with all imaging methods were presented to each rater simultaneously. STN and GPi were identified by using their relative position to the anterior commissure–posterior commissure line and their signal intensity, which was reported to be hypointense to normal-appearing white matter (hereafter, hypointense) on T2w (9), T2*w, phase, and SW images (21) and was expected to be hyperintense to normal-appearing white matter (hereafter, hyperintese) on R2* and QSM images because of iron deposition. STN and GPi visualization scores were assigned to each imaging method. For STN, a score of 0 indicated STN was not visible; a score of 1, the STN-SN complex was poorly visible with fuzzy borders; a score of 2, only the superior border of STN and not the border with SN was visible; and a score of 3, STN was well defined and clearly differentiable from its superior neighbor, presumably ZI, and its inferior neighbor, SN. For GPi, a score of 0 indicated the GPi was not visible; a score of 1, the globus pallidus was poorly visible with fuzzy borders; a score of 2, the GPi was clearly differentiable from the internal capsule (IC) but not from the external globus pallidus (GPe); a score of 3, the GPi was clearly differentiable from both the IC and the GPe, but the medial medullary lamina between the GPi and GPe was vague; and a score of 4, the medial medullary lamina was clearly defined. We also recorded the sections on which STN and GPi were best depicted for subsequent quantitative analysis.

Quantitative Image Analysis

A third resident radiologist (A.D.S., 3 years of experience) measured the CNR of the STN and GPi on all of the images. For each subject, bilateral regions of interest were manually drawn on the single section recorded from the previous qualitative assessment on the image with the highest visualization score (Fig 1). After delineating the STN, a 2-mm band tracing the superior border of the STN and a 1-mm band tracing the inferior border of the STN were drawn to calculate the intensity difference between the STN and its superior neighbor, presumably the ZI, and its inferior neighbor, SN. Similarly, after delineating the GPi, a 2-mm band tracing the medial border of the globus pallidus and a 1-mm band tracing the lateral border of the GPi were drawn to calculate the intensity difference between the GPi and the IC, as well as the difference between the GPi and the GPe. In addition, a 50-mm^2 circular region of interest was placed in the medial dorsal aspect of the thalamus. T2w and T2w* images were used to confirm the anatomic locations of these regions of interest and served as arbitrators to decide the image to draw on when multiple images had the same highest score. These regions of interest were then propagated onto the complete set of images (T2w, T2*w, R2*, phase, SW, and QSM images). Contrast on each image was calculated as the absolute difference between the mean value in the STN and GPi (including both left and right sides) and the mean value

Figure 1

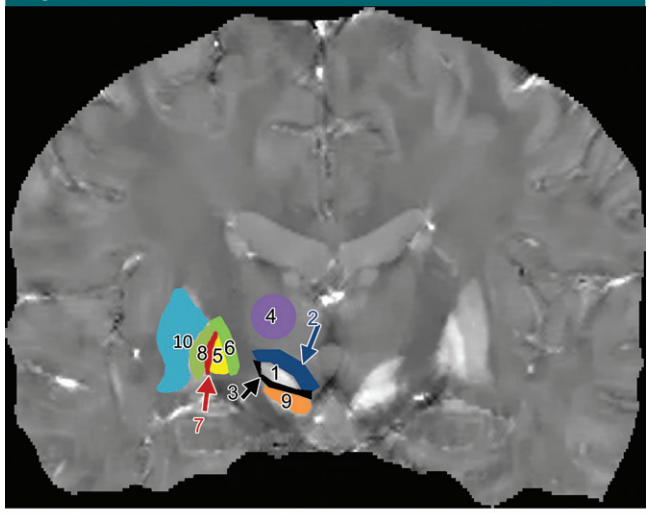

a.

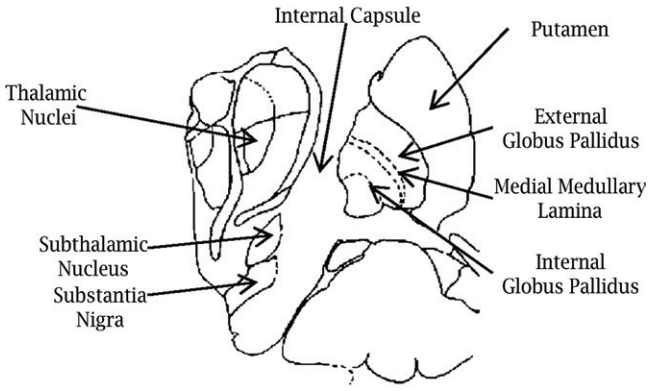

b.

Figure 1: Examples of region of interest delineation in a healthy 27-year-old male volunteer. **(a)** Coronal QSM image shows the STN *(1)*; its superior neighbor, presumably the ZI *(2)*; the border between the STN and the SN *(3)*; the thalamus *(4)*; the GPi *(5)*; the IC *(6)*; the border between the GPi and the GPe, presumably the medial medullary lamina *(7)*; and the GPe *(8)*. Other visible anatomic regions included the SN *(9)* and the putamen *(10)*. **(b)** Corresponding frontal sections on a Schaltenbrand and Wahren atlas along the anteroposterior axis show a section 2 mm anterior to the midcommissural point.

in the surrounding bands. Noise was measured by calculating the standard deviation of the signal intensity in the thalamus due to its relatively uniform signal intensity.

Statistical Analysis

To assess the interrater agreement in each imaging method, a percentage of agreement was calculated as the number of subjects who received identical scores from both raters divided by the total number of subjects ($n = 18$) for each imaging method. For visualization scores and CNR measurements, Wilcoxon rank sum tests and Wilcoxon signed rank tests, respectively, were performed by using all 18 subjects to test the differences between QSM and each of the other imaging methods. A P value of less than .05 was considered statistically significant. These statistical analyses were performed with SPSS for Windows (version 16.0; SPSS, Chicago, Ill).

Results

Imaging was successful in all 18 subjects. The STN appeared hypointense and lenticular on T2w and T2*w images, with hypointense line segments on phase and SW images and hyperintense line segments on R2* and QSM images (Fig E1 [online]). The GPi appeared hypointense on T2W, T2*W, and SW images; heterogeneous on phase images; and hyperintense on R2* and QSM images. Statistics of the visualization score from two raters are presented in Figure E2 (online). The average visualization scores for STN for the two readers for T2w, T2*w, R2*, phase, SW, and QSM images were 1.61, 1.42, 1.42, 2.39, 2.22, and 2.94, respectively, For GPi, the average visualization scores were 1.78, 1.89, 2.19, 1.69, 2.17, and 3.42, respectively. All the differences between QSM images and the other images were significant ($P < .01$). For STN scores, the percentage of agreement between the two raters was 55.6%, 44.4%, 50.0%, 61.1%, 22.2%, and 88.9% for the 18 subjects for T2w, T2*w, R2*, phase, SW, and QSM images, respectively. For GPi scores, the percentage of agreement was 33.3% for all of the imaging methods except QSM; the agreement for QSM was 50%.

Although phase and SW imaging had high visualization scores similar to the visualization score of QSM for STN depiction, the hypointense line segments on phase and SW images did not correspond to STN when compared with the T2*w image, as exemplified in Figure 2. Instead, QSM was used to correctly locate STN, as confirmed with the T2*w and T2w images. Substantial blurring was seen on the R2* image. It should be noted that T2*w, R2*, phase, SW, and QSM images were derived from an identical data set that was naturally coregistered.

Statistics of the CNR measurements are presented in Figure E3 (online) and the Table. QSM yields the best CNR for STN and GPi depiction in each category (STN-ZI, STN-SN, GPi-IC, and GPi-GPe), and the differences were significant between QSM and other imaging methods

Figure 2

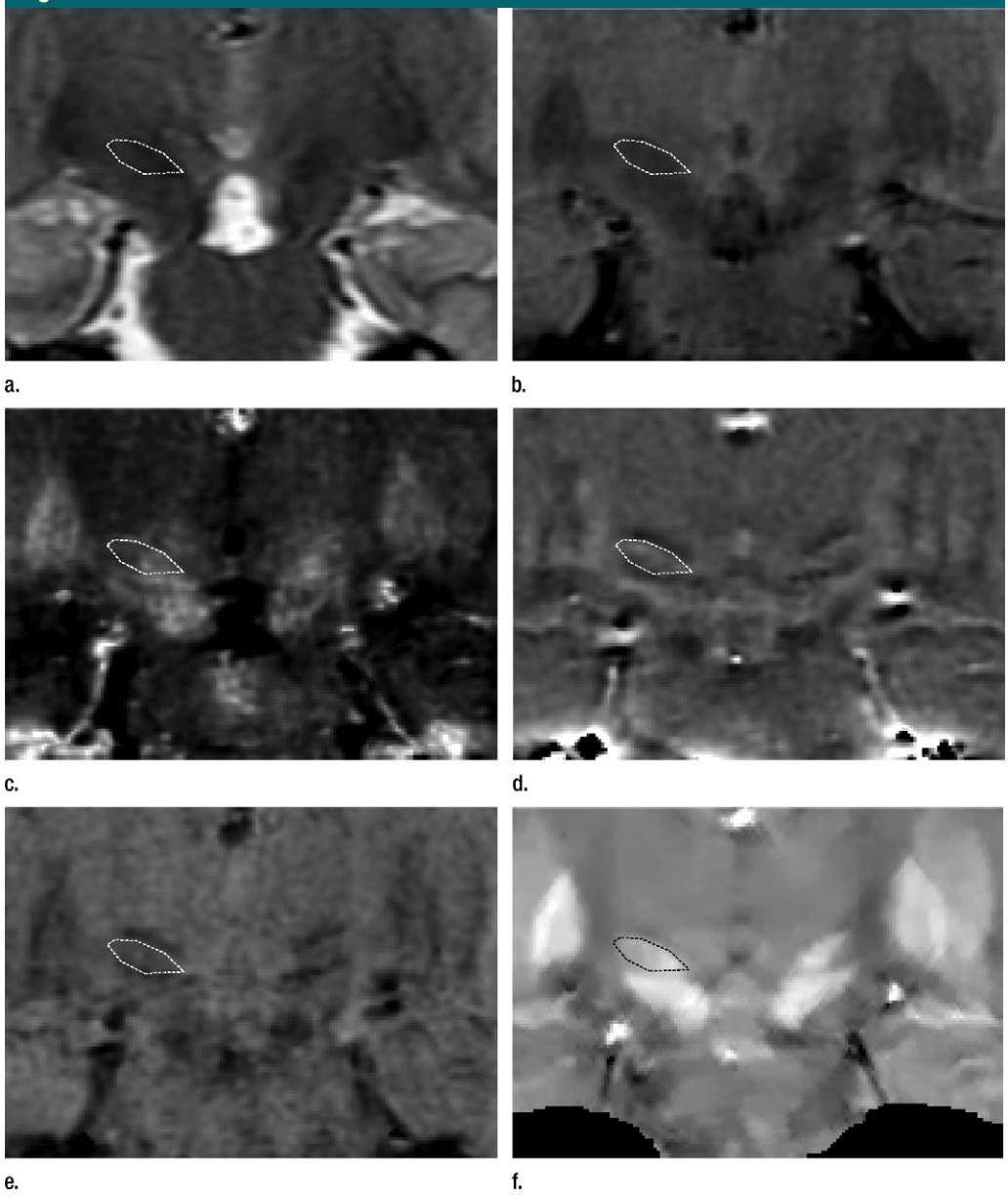

Figure 2: STN (outlined area) and GPi region in a healthy 25-year-old female volunteer. **(a)** T2w, **(b)** T2*w, **(c)** R2*, **(d)** phase, **(e)** SW, and **(f)** QSM images. In **d** and **e**, the STN regions were vertically interposed between hypointense line segments, and the STN region itself appeared isointense to its horizontal neighbor, IC.

in each category ($P < .01$). When compared with the median CNR on conventional T2w images, median CNR on QSM images was 6.4 and 10.7 times higher for differentiation of STN from ZI and SN, respectively, and it was 22.7 and 9.1 times higher for differentiation of GPi from IC and GPe, respectively.

Discussion

Our results indicate that QSM images yielded a superior CNR in the depiction of the STN and GPi when directly compared with T2w, T2*w, R2*, phase, and SW images. Both STN and GPi appeared hyperintense on QSM images. QSM reliably reflected the true lenticular shape of the STN and enabled us to clearly differentiate it from the ZI superior to it and discernibly distinguish it from the SN inferior to it. The improved depiction of the STN and GPi on QSM images may improve neurosurgical targeting and surgical planning for deep brain

CNR Measurements

CNR	T2w Image	T2*w Image	R2* Image	Phase Image	SW Image	QSM Image
STN-ZI						
Median	1.56	2.71	3.00	2.03	0.66	9.97
Interquartile range	0.95–1.97	2.15–3.06	2.38–4.57	1.30–2.76	0.45–0.97	8.34–11.9
Range	0.01–2.84	1.15–5.51	1.86–7.91	0.70–3.22	0.18–3.01	6.06–19.6
STN-SN						
Median	0.29	0.48	0.54	1.54	0.93	3.11
Interquartile range	0.10–0.79	0.14–0.78	0.26–1.32	1.03–2.32	0.49–1.25	2.31–4.66
Range	0.01–1.51	0.04–2.04	0.04–3.04	0.54–3.19	0.17–1.39	1.68–10.5
GPi-IC						
Median	0.75	3.01	5.3	1.76	2.95	16.96
Interquartile range	0.12–0.99	2.53–4.17	3.08–6.60	0.65–2.81	2.47–3.64	10.5–21.4
Range	0.04–2.05	0.69–6.06	1.48–8.38	0.32–4.2	0.95–4.52	5.92–38.1
GPi-GPe						
Median	0.26	0.59	0.89	0.76	0.51	2.33
Interquartile range	0.15–0.87	0.3–1.02	0.33–1.4	0.36–1.26	0.15–0.79	1.48–2.93
Range	0.01–1.38	0.03–1.76	0.08–2.59	0.16–2.32	0.04–1.65	1.15–4.97

stimulator placement used to treat Parkinson disease and dystonia.

There are several benefits for patients who are undergoing deep brain stimulation that are provided by accurate direct depiction of the STN. Because of the poor to moderate contrast of the STN in current preoperative imaging, intraoperative electrophysiologic exploration (22) is performed by using microelectrodes and analysis of firing patterns to confirm that the target has electrical activity characteristic of the STN. This approach requires the patient to participate in the surgery; therefore, he or she must be awake and cooperative. Multiple passes with the microelectrode are usually preformed during electrophysiologic STN localization; these are time consuming and result in disruption of normal tissue. QSM enables improved preoperative STN depiction, and this technique can be imported into existing stereotactic localization software. Further patient studies may show that improved depiction could result in a more reliable stereotactic target, a decreased number of exploratory passes, and an increased rate of optimal electrode placement. Reliable imaging of STN may ultimately lead to safer more efficacious surgery in a larger group of patients who may have been unable or unwilling to undergo conscious surgery.

The improved CNR of QSM compared with that attained with relaxation-based methods, such as T2w, may be explained by the different mechanisms of signal generation. In relaxation-based methods, the signal comes from the precession of water protons after RF excitation and then gradually decays at a relaxation rate according to the local molecular environment. Since water protons are relatively uniformly distributed across normal brain parenchyma (23), the contrast between structures actually originates from differences in decaying rates, which are small. However, in QSM, tissue magnetic susceptibility largely reflects the concentration of paramagnetic unpaired electrons in tissue. Only certain metallic elements of biomolecules, such as highly paramagnetic iron, have unpaired electrons that are very selectively deposited in cerebral structures (24). Thus, QSM is sensitive in the depiction of brain structures with iron deposition, such as the STN or GPi (9,25).

The improved CNR of QSM compared with the CNR attained with traditional methods that use susceptibility effects, such as T2*w, R2*, phase, and SW imaging, is expected because of the underlying physics. The *phase* in phase imaging reflects the magnetic field that is generated by susceptibility sources surrounding the observation point, and it is a nonlocal quantity. The T2*w, R2*, and SW contrasts reflect the intravoxel variance of the magnetic field, which is also nonlocal. The phase and SW images, having large blooming artifacts, enable easy visualization of STN. However, these blooming artifacts depend on the object's orientation, geometry, and various imaging parameters, and they typically appear at interfaces perpendicular to the main magnetic field (26). These blooming artifacts, which render tissue border definition difficult, are especially undesirable in surgical planning. The dorsolateral aspect of STN, which was found to be the ideal target (27), is close to the interface. These blooming artifacts can be removed through deconvolution with a unit magnetic dipole field, which is performed during QSM to reflect local tissue susceptibility.

In this study, there were several technical improvements compared with previous attempts. Direct visualization of STN with QSM has been explored at 7 T (11) and 1.5 T (28). However, the study performed by Schafer et al (11) either requires multiple orientation sampling (29) or allows a small field of view specific for only

the STN. The susceptibility map reconstructed by O'Gorman et al (28) was largely corrupted by noise, preventing meaningful CNR measurements. Here, the QSM images were reconstructed from one acquisition by using the morphology-enabled dipole inversion approach (14,15,20). A global field of view of the brain parenchyma shown here offered better landmarks for locating the STN and other targeting sites for deep brain stimulation, such as the GPi. The global view also makes it easier to integrate the QSM images into other image viewers or navigation systems commonly used in deep brain stimulation.

A few limitations must be acknowledged. The number of patients in this study was small and, consequently, the results suggesting improved depiction of STN and GPi on QSM images will need to be studied in a larger independent sample of patients before any general conclusions can be drawn regarding improvements in neurosurgical planning and evaluation of the brain in patients with Parkinson disease. The visualization scores used in this study do not correspond to any clinical metric, and they served as a qualitative measure for image comparison. MR imaging inherently is a motion-sensitive imaging modality; thus, QSM images may be degraded by motion. Another limitation of the QSM technique is that only brain parenchyma is retained; skull stripping is performed to eliminate signal void regions, such as cortical bone or air, that lead to large noise propagation at QSM. Nevertheless, QSM images are acquired concurrently with T2*w images; therefore, QSM images may be overlaid onto T2*w images for additional anatomic landmarks, such as the skull. Lastly, QSM takes approximately 20 minutes to postprocess, which leaves room for technical improvement for faster reconstructions (30).

In summary, QSM improves visualization and the CNR of the STN significantly better than the current standard-of-care MR imaging sequences and can be used to better localize the STN for the deep brain stimulator placement used to treat Parkinson disease.

Disclosures of Conflicts of Interest: T.L. Financial activities related to the present article: none to disclose. Financial activities not related to the present article: is listed as an inventor on patent applications related to the QSM technique. Other relationships: none to disclose. **S.E.** No relevant conflicts of interest to disclose. **A.S.** No relevant conflicts of interest to disclose. **W.C.** No relevant conflicts of interest to disclose. **M.G.K.** No relevant conflicts of interest to disclose. **A.J.T.** No relevant conflicts of interest to disclose. **Y.W.** Financial activities related to the present article: none to disclose. Financial activities not related to the present article: is listed as an inventor on patent applications related to the QSM technique. Other relationships: none to disclose.

References

1. Benabid AL, Chabardes S, Mitrofanis J, Pollak P. Deep brain stimulation of the subthalamic nucleus for the treatment of Parkinson's disease. Lancet Neurol 2009; 8(1):67–81.
2. Limousin P, Krack P, Pollak P, et al. Electrical stimulation of the subthalamic nucleus in advanced Parkinson's disease. N Engl J Med 1998;339(16):1105–1111.
3. Herzog J, Fietzek U, Hamel W, et al. Most effective stimulation site in subthalamic deep brain stimulation for Parkinson's disease. Mov Disord 2004;19(9):1050–1054.
4. Guehl D, Cuny E, Benazzouz A, et al. Side-effects of subthalamic stimulation in Parkinson's disease: clinical evolution and predictive factors. Eur J Neurol 2006;13(9):963–971.
5. McIntyre CC, Mori S, Sherman DL, Thakor NV, Vitek JL. Electric field and stimulating influence generated by deep brain stimulation of the subthalamic nucleus. Clin Neurophysiol 2004;115(3):589–595.
6. Tamma F, Caputo E, Chiesa V, et al. Anatomoclinical correlation of intraoperative stimulation-induced side-effects during HF-DBS of the subthalamic nucleus. Neurol Sci 2002; 23(Suppl 2):S109–S110.
7. Lang AE, Houeto JL, Krack P, et al. Deep brain stimulation: preoperative issues. Mov Disord 2006;21(Suppl 14):S171–S196.
8. Massey LA, Miranda MA, Zrinzo L, et al. High resolution MR anatomy of the subthalamic nucleus: imaging at 9.4 T with histological validation. Neuroimage 2012;59(3): 2035–2044.
9. Dormont D, Ricciardi KG, Tandé D, et al. Is the subthalamic nucleus hypointense on T2-weighted images? a correlation study using MR imaging and stereotactic atlas data. AJNR Am J Neuroradiol 2004;25(9):1516–1523.
10. Cho ZH, Min HK, Oh SH, et al. Direct visualization of deep brain stimulation targets in Parkinson disease with the use of 7-tesla magnetic resonance imaging. J Neurosurg 2010; 113(3):639–647.
11. Schäfer A, Forstmann BU, Neumann J, et al. Direct visualization of the subthalamic nucleus and its iron distribution using high-resolution susceptibility mapping. Hum Brain Mapp 2012;33(12):2831–2842.
12. Breit S, LeBas JF, Koudsie A, et al. Pretargeting for the implantation of stimulation electrodes into the subthalamic nucleus: a comparative study of magnetic resonance imaging and ventriculography. Neurosurgery 2006; 58(1 Suppl):ONS83–ONS95.
13. de Rochefort L, Liu T, Kressler B, et al. Quantitative susceptibility map reconstruction from MR phase data using bayesian regularization: validation and application to brain imaging. Magn Reson Med 2010; 63(1):194–206.
14. Liu J, Liu T, de Rochefort L, et al. Morphology enabled dipole inversion for quantitative susceptibility mapping using structural consistency between the magnitude image and the susceptibility map. Neuroimage 2012; 59(3):2560–2568.
15. Liu T, Liu J, de Rochefort L, et al. Morphology enabled dipole inversion (MEDI) from a single-angle acquisition: comparison with COSMOS in human brain imaging. Magn Reson Med 2011;66(3):777–783.
16. Schweser F, Deistung A, Lehr BW, Reichenbach JR. Quantitative imaging of intrinsic magnetic tissue properties using MRI signal phase: an approach to in vivo brain iron metabolism? Neuroimage 2011;54(4):2789–2807.
17. Volz S, Hattingen E, Preibisch C, Gasser T, Deichmann R. Reduction of susceptibility-induced signal losses in multi-gradient-echo images: application to improved visualization of the subthalamic nucleus. Neuroimage 2009;45(4):1135–1143.
18. Wang Y, Yu Y, Li D, et al. Artery and vein separation using susceptibility-dependent phase in contrast-enhanced MRA. J Magn Reson Imaging 2000;12(5):661–670.
19. Deistung A, Rauscher A, Sedlacik J, Stadler J, Witoszynskyj S, Reichenbach JR. Susceptibility weighted imaging at ultra high magnetic field strengths: theoretical considerations and experimental results. Magn Reson Med 2008;60(5):1155–1168.
20. Liu T, Wisnieff C, Lou M, Chen W, Spincemaille P, Wang Y. Nonlinear formulation of the magnetic field to source relationship for robust quantitative susceptibility mapping. Magn Reson Med 2013;69(2):467–476.

21. Vertinsky AT, Coenen VA, Lang DJ, et al. Localization of the subthalamic nucleus: optimization with susceptibility-weighted phase MR imaging. AJNR Am J Neuroradiol 2009; 30(9):1717–1724.

22. Gross RE, Krack P, Rodriguez-Oroz MC, Rezai AR, Benabid AL. Electrophysiological mapping for the implantation of deep brain stimulators for Parkinson's disease and tremor. Mov Disord 2006;21(Suppl 14):S259–S283.

23. Just M, Thelen M. Tissue characterization with T1, T2, and proton density values: results in 160 patients with brain tumors. Radiology 1988;169(3):779–785.

24. Langkammer C, Schweser F, Krebs N, et al. Quantitative susceptibility mapping (QSM) as a means to measure brain iron? a post mortem validation study. Neuroimage 2012;62(3):1593–1599.

25. Rutledge JN, Hilal SK, Silver AJ, Defendini R, Fahn S. Study of movement disorders and brain iron by MR. AJR Am J Roentgenol 1987;149(2):365–379.

26. Li J, Chang S, Liu T, et al. Reducing the object orientation dependence of susceptibility effects in gradient echo MRI through quantitative susceptibility mapping. Magn Reson Med 2012;68(5):1563–1569.

27. Lanotte MM, Rizzone M, Bergamasco B, Faccani G, Melcarne A, Lopiano L. Deep brain stimulation of the subthalamic nucleus: anatomical, neurophysiological, and outcome correlations with the effects of stimulation. J Neurol Neurosurg Psychiatry 2002;72(1): 53–58.

28. O'Gorman RL, Shmueli K, Ashkan K, et al. Optimal MRI methods for direct stereotactic targeting of the subthalamic nucleus and globus pallidus. Eur Radiol 2011; 21(1):130–136.

29. Liu T, Spincemaille P, de Rochefort L, Kressler B, Wang Y. Calculation of susceptibility through multiple orientation sampling (COSMOS): a method for conditioning the inverse problem from measured magnetic field map to susceptibility source image in MRI. Magn Reson Med 2009; 61(1):196–204.

30. Schweser F, Deistung A, Sommer K, Reichenbach JR. Toward online reconstruction of quantitative susceptibility maps: superfast dipole inversion. Magn Reson Med 2012 Jul 12. [Epub ahead of print]